ARTICLES
https://doi.org/10.1038/s41560-020-00702-8

nature energy

Ultralight and fire-extinguishing current collectors for high-energy and high-safety lithium-ion batteries

Yusheng Ye[1,4], Lien-Yang Chou[1,4], Yayuan Liu[1], Hansen Wang[1], Hiang Kwee Lee[1], Wenxiao Huang[1], Jiayu Wan[1], Kai Liu[1], Guangmin Zhou[1], Yufei Yang[1], Ankun Yang[1], Xin Xiao[1], Xin Gao[1], David Thomas Boyle[2], Hao Chen[1], Wenbo Zhang[1], Sang Cheol Kim[1] and Yi Cui[1,3] ✉

Inactive components and safety hazards are two critical challenges in realizing high-energy lithium-ion batteries. Metal foil current collectors with high density are typically an integrated part of lithium-ion batteries yet deliver no capacity. Meanwhile, high-energy batteries can entail increased fire safety issues. Here we report a composite current collector design that simultaneously minimizes the 'dead weight' within the cell and improves fire safety. An ultralight polyimide-based current collector (9 μm thick, specific mass 1.54 mg cm^{-2}) is prepared by sandwiching a polyimide embedded with triphenyl phosphate flame retardant between two superthin Cu layers (~500 nm). Compared to lithium-ion batteries assembled with the thinnest commercial metal foil current collectors (~6 μm), batteries equipped with our composite current collectors can realize a 16–26% improvement in specific energy and rapidly self-extinguish fires under extreme conditions such as short circuits and thermal runaway.

Lithium-ion batteries (LIB) are a ubiquitous technology in modern human civilization, powering devices such as portable electronics, electric vehicles and grid energy storage. The rapid development of smart devices has revitalized worldwide efforts towards pursuing higher energy and safer LIB. Commercial current collectors (CCs) are conductive metal foils made of high-density materials such as copper (density 8.96 g cm^{-3}) or aluminium (density 2.70 g cm^{-3}) and account for ~15–50 wt% of the total weight of LIB[1]. Although CCs in batteries play a critical role in efficient electron transfer and mechanical support for electrode materials (Fig. 1), they are generally inactive components that cause considerable dead weight yet do not contribute to cell capacity. Thus, the battery industry is constantly trying to decrease the thickness of these metal foils to achieve a lightweight CC. However, such attempts have demonstrated undesirable deterioration in the mechanical behaviour of CCs. The recent advent of novel CCs includes three-dimensional (3D) porous metal CCs for fast battery charging[2,3], 3D graphene foam for flexible LIB[4,5], two-dimensional metal mesh for high-rate LIB[6] and two-dimensional carbon-based CCs for LIB[1,7,8]. However, these designs are hindered by, variously, poor mechanical behaviour, a need for additional electrolytes, high cost, poor scalability and chemical instability. Moreover, titanium nitride-coated polyimide (PI) CCs have been investigated in aluminium-ion batteries as a means to protect aluminium CCs from oxidation[9], but it is unclear how the PI-composite CCs affect the battery performance. In spite of the efforts made so far, battery energy remains limited due to the lack of lightweight and robust CCs, thus calling for new approaches.

Additionally, high-energy LIB entail serious safety concerns due to the use of highly flammable organic electrolytes and polyolefin separators[10,11]. During shorting, overcharging, exposure to high temperature (>150 °C) or other thermal abuse conditions, exothermic reactions readily occur. This release of energy, which causes separator shrinkage and the solid electrolyte interface or electrolyte to decompose, can set off a chain of additional exothermic reactions leading to thermal runaway, fires and explosions[12–14]. In addition, the breakdown of electrodes (especially metal oxide materials) can exacerbate battery fires by providing an additional oxygen source[15,16]. Safe battery operation is thus a critical prerequisite for practical application of high-energy LIB. So far, considerable efforts have been dedicated to exploring safer batteries, including embedding flame-retardant materials into separators, electrolytes and/or electrodes, as well as the use of ceramic particle coatings[17–22]. Using such cell flame retardants or additives can improve safety to a certain extent, but their use inevitably affects electron/ion transport and introduces extra weight. Replacing the electrolyte solvent with non-flammable molecules, increasing the concentration of lithium salts and adopting solid-state electrolytes can also help to formulate safe batteries[23–28]. However, these strategies generally severely compromise battery performance by increasing electrolyte viscosity, decreasing lithium ion conductivity, altering the operating voltage or degrading the mechanical integrity of the separator. Modified CCs with positive temperature coefficients have also been proposed to shut down the batteries when temperatures increase[29–31]. However, high leakage current, reduced electrical conductivity and increased CC weight issues in turn reduce the performance. When considering improvements to high-energy LIB, few studies have investigated simultaneously advancing performance and safety.

Here, we propose an ultralight PI-based CC with fire-extinguishing properties that simultaneously minimizes the dead weight and enhances the safety of LIB. Our CC is fabricated by embedding triphenyl phosphate (TPP) flame retardant into

[1]Department of Materials Science and Engineering, Stanford University, Stanford, CA, USA. [2]Department of Chemistry, Stanford University, Stanford, CA, USA. [3]Stanford Institute for Materials and Energy Sciences, SLAC National Accelerator Laboratory, Menlo Park, CA, USA. [4]These authors contributed equally: Yusheng Ye, Lien-Yang Chou. ✉e-mail: yicui@stanford.edu

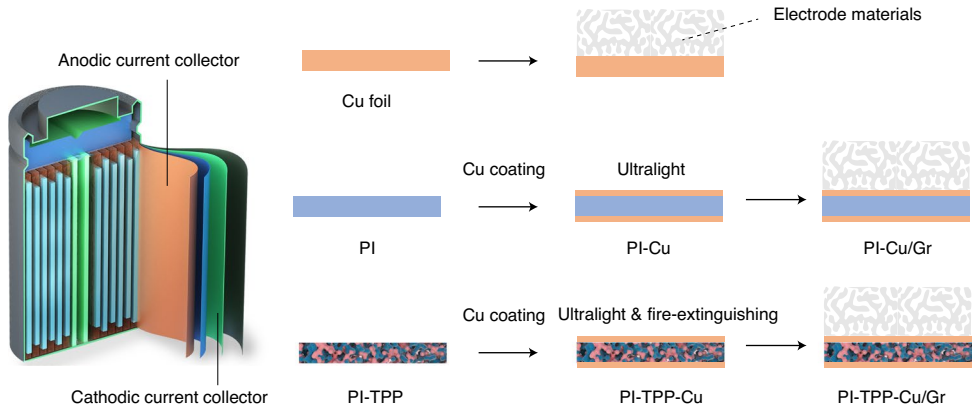

Fig. 1 | Conventional CCs and our design. Conventional pure Cu CCs are heavy and bulky, while PI-Cu CCs are much lighter. By incorporating TPP and subsequently coating the CC with ultrathin Cu layers on both sides, the resulting PI-TPP-Cu CC is ultralight and exhibits efficient flame retardant properties.

lightweight PI films, followed by coating two ultrathin external metal layers (for instance, a ~500 nm layer of Cu) on both sides to impart high electrical conductivity. This CC possesses a mass loading of only ~1.54 mg cm^{-2}, which is, notably, seven times lighter than normal commercial Cu foil CCs. When compared to LIB fabricated using the thinnest Cu CCs (~6 µm thick with a mass loading of 5.38 mg cm^{-2}), batteries assembled with our composite CCs can be improved by ~16–26% in specific energy. This design isolates the flame retardant from the LIB electron/ion pathway and chemical reactions, maintains the stability of normal cell operation and allows fast and efficient self-extinguishing of battery fires in the event of thermal runaway. Our ultralight and flame-retardant-embedded CC therefore concurrently improves the specific energy and critical safety of LIB.

CC configuration and characterization

As illustrated schematically in Fig. 1, we have selected PI as the CC supporting film due to its low density, superior mechanical properties, good resistance to solvents, excellent thermal stability (>400 °C) and remarkable flame resistance. The support PI film was prepared with a modified PI synthesis process utilizing pyromellitic anhydride, 4,4′-oxydianiline and 1,4-bis(4-amino-2-trifluoromethyl-phenoxy)benzene. This synthesis ensures high thermal stability (>550 °C) compared to common PIs[32,33]. The detailed synthesis process can be found in Supplementary Fig. 1. Notably, many different PIs can serve as the support substrate in this CC design, some of which are listed in Supplementary Table 1. In order to maximize the mechanical performance of the CC, a non-porous PI was synthesized[34]. The flame retardant was mixed with the PI precursor and then heated to form the composite supporting film. TPP was selected as the flame-retardant material since it is halogen-free, low-cost and one of the most efficient and environmentally friendly flame retardants with a low melting point (~48–50 °C)[35]. The relatively low melting point of TPP reduces the response time in the event of a fire.

Scanning electron microscopy (SEM) images show that the PI structure maintains the same cross-sectional thickness of 8 µm before (Fig. 2a) and after incorporating TPP (PI-TPP, Fig. 2b). Here, TPP increases the uniformity of the PI-TPP film. The difference in the morphology stems from the solvent-soluble feature and phase change of TPP during synthesis, whereby TPP solidifies within the PI when cooled to room temperature, as is evident from the different colour of PI-TPP in Supplementary Fig. 2. Besides, pre-mixing the TPP/PI precursors blend during synthesis contributes to a homogeneous TPP distribution. Before metal coating, we used O_2 plasma to treat the supporting film (either PI or PI-TPP), rendering the surface highly hydrophilic to enhance surface adhesion. Using magnetron sputtering deposition, two 500 nm ultrathin external metal layers (for instance, Cu) are deposited on both sides to function as the conductive layers (Fig. 2c) of our composite CC (PI-Cu or PI-TPP-Cu). These metal conductive layers demonstrate good homogeneity, which provides good electrical conductivity of the CC.

In contrast to previous implementations of in-cell flame retardants, our design encapsulating the flame retardant in the CC eliminates potential negative impacts on electron/ion transport and side reactions. Tape peel testing reveals that the metal layer is strongly adhered to the substrate, as shown in Supplementary Fig. 3 and Supplementary Video 1. Notably, PI is cost-effective and the metal deposition can be achieved by scalable methods such as electroless metal plating[36] and sputtering[37]. As a proof of concept, we fabricated a PI-TPP-Cu CC with a size of 8 cm × 8 cm (Supplementary Fig. 4).

We used thermogravimetric analysis (TGA) to study the TPP content in PI-TPP films with a fixed thickness of 8 µm at various TPP loadings (Fig. 2d). TPP begins to decompose at ~250 °C and is completely removed from the sample by 350 °C, while the decomposition of PI mainly occurs between ~550 and ~650 °C. Based on the TGA results, the TPP contents of two films were determined to be ~15 wt% and 25 wt%, which are close to the actual amounts added. When the theoretical TPP content is further increased to ~30–50 wt%, the TGA curves overlap and the actual amount of TPP present in the PI-TPP composites remains constant at 25 wt%, as shown in Supplementary Fig. 5. To give insight into the underlying mechanism governing the TPP content, X-ray photoelectron spectroscopy (XPS) depth profiling was carried out to examine the distribution of TPP within the PI film (Supplementary Fig. 6). Prior to sputtering, no P2p XPS signal originating from TPP is detected. Subsequent sputtering of the PI-TPP film reveals the presence of TPP within the PI film, as is evident from the emergence of characteristic P2p XPS peaks. These results demonstrate that a surface layer of TPP may form on the composite film when excess TPP (>25 wt%) is added during the synthesis. The surface TPP is expected to evaporate much more easily compared to the encapsulated internal TPP. Fourier transform infrared spectroscopy (FTIR) spectra are recorded to further confirm the existence of TPP in the PI-TPP composite, as shown in Fig. 2e. The peaks at 1,294 cm^{-1} can be assigned to the vibrational mode of P=O in pentavalent phosphorus compounds, while the peaks at 953 cm^{-1} can be assigned to the P–O groups present in TPP[38].

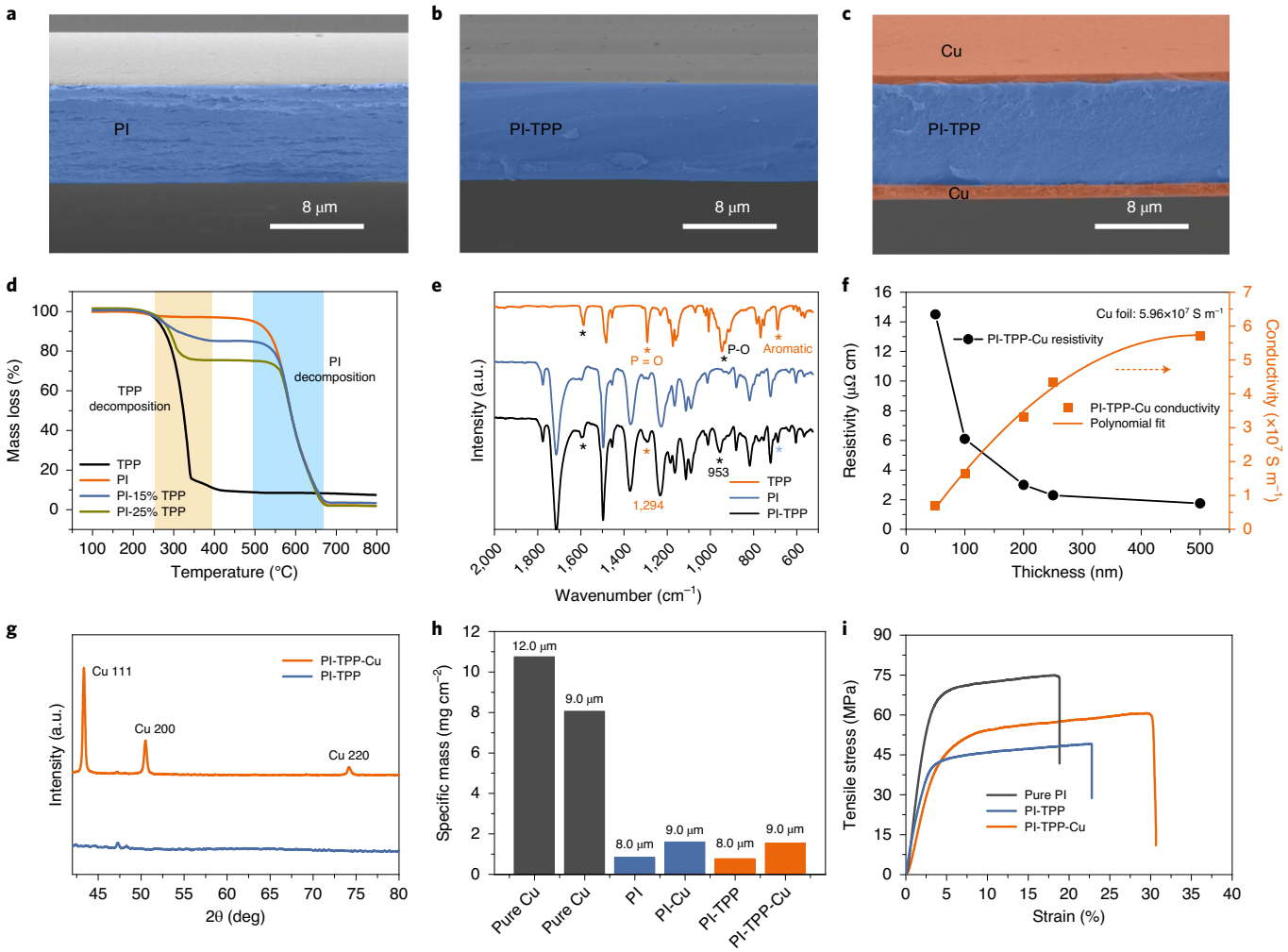

Fig. 2 | Materials fabrication and structural characterization of PI-based CCs. a–c, Cross-sectional SEM images of PI (**a**), PI-TPP (**b**) and PI-TPP-Cu (**c**) films. **d**, TGA demonstrates the TPP contents in the PI-TPP composites. TPP begins to decompose at ~250 °C and is completely removed from the sample by 350 °C (yellow shading), while the decomposition of PI mainly occurs between ~550–650 °C (blue shading). **e**, FTIR spectra of the as-obtained PI, TPP and PI-TPP composites. The asterisks represent the characteristic peaks of TPP. **f**, Correlation between the resistivity of CC and the thickness of the Cu conductive layer. The fit to the conductivity curve is obtained by polynomial fitting. When the Cu thickness reaches 500 nm, the conductivity is close to that of commercial Cu foil. **g**, XRD analysis of the PI-TPP and PI-TPP-Cu composites. **h**, Specific mass comparison between the Cu foil, PI-TPP and PI-TPP-Cu CC. The ultralight PI-based CC can significantly increase the specific energy of LIB. **i**, Specific tensile strength of different PI-based films.

The key factor in tuning the electrical conductivity of the CCs relies on the conducting layers on the composite CC surfaces. Thus, we further studied the relationship between Cu thickness and the resistivity of the PI-TPP-Cu CC (Fig. 2f). As Cu thickness increases, the resistivity of CC on the same side decreases due to more effective connections on the Cu conductive layer. Here, we chose a 500 nm Cu deposition layer for subsequent experiments to ensure an electrical conductivity of 5.71×10^7 S m^{-1} while minimizing the weight of the CC. One advantage of this design is that we can regulate the thickness of the CC by changing the thickness of the PI or PI-TPP supporting film without affecting the electricial conductivity of CC, as the Cu thickness is not changing. XRD patterns (Fig. 2g) demonstrate strong characteristic peaks assignable to Cu, affirming the successful Cu coating on the PI-TPP film. The dense copper coating layer can prevent TPP from dissolving into the electrolyte.

Figure 2h shows the specific masses of the Cu foil, PI-Cu and PI-TPP-Cu CCs. Generally, the specific masses of a 12.0 μm and a 9.0 μm thick commercial Cu foil CC are ~10.75 mg cm^{-2} and 8.06 mg cm^{-2}, respectively, constituting ~25–35% of the overall weight of an anode. Replacing Cu foil with a PI-Cu CC notably reduces the CC mass loading to 1.60 mg cm^{-2}, which is only ~3–5% of the total electrode weight. Further incorporating TPP into PI and coating Cu on the surfaces to form PI-TPP-Cu does not obviously change the specific mass of PI-TPP-Cu CC (~1.54 mg cm^{-2}). The slight decrease in specific mass is due to TPP having a lower theoretical density (1.18 g cm^{-3}) than PI (~1.42 g cm^{-3}). Even compared with the thinnest Cu CC (~6 μm thick, 5.38 mg cm^{-2}) used in current LIB, our composite CC demonstrates a notable 3.5× lighter specific mass. Owing to the use of PI as a mechanical support, our PI-TPP-Cu composite CC shows good mechanical performance (Fig. 2i). The incorporation of TPP into PI only slightly decreases the mechanical strength compared to the pure PI. More interestingly, the 9.0 μm thick PI-TPP-Cu CC displays comparable mechanical behaviour (Young's modulus: 2.01 GPa) to that of commercial Cu CCs (see Supplementary Fig. 7), which is promising for practical applications. Supplementary Fig. 8 depicts the overall fabrication process of a PI-TPP-Cu-based electrode. Various electrode materials can be coated onto our PI-TPP-Cu composite CC to form different anodic electrodes.

Fire retardancy and battery performance

We first coated graphite (Gr) electrodes on commercial Cu foil and PI-TPP-Cu CCs (9 μm thick) to evaluate the flame retardancy of the electrode. A vertical fire-extinguishing experiment was used to evaluate the burning capacity of the obtained Gr electrode. As shown in Supplementary Fig. 9, the pure PI-TPP-Cu/Gr anode does not catch fire when directly exposed to a flame. To more realistically mimic the combustion of batteries under extreme conditions, we added a predefined amount 1.0 M $LiPF_6$ in ethylene carbonate/diethyl carbonate (EC/DEC, 1:1 in volume) electrolyte to the electrodes and rested them for 12 h to ensure complete wetting by the electrolyte. Self-extinguishing time (SET) values, which describe the burn duration of an ignited sample, are used to quantify the flame retardancy. SET values are calculated by considering the mass of electrolyte maintained after resting (details in Methods)[21,22]. The SET of a commercial Cu CC/graphite (Cu/Gr) electrode soaked with electrolyte is ~83.3 s g^{-1}, while the SET value of an electrode based on PI-Cu (without TPP; PI-Cu/Gr) was decreased to 58.3 s g^{-1}. This is because the combustion of PI at high temperatures will generate CO_2, which will in turn dilute the O_2 content near the burning interface. Increasing the TPP content in the PI further enhances the fire retardancy, as shown in Fig. 3a. As the TPP content increases from 0 wt% to 25 wt%, the SET value decreases linearly and achieves a small SET value of 18.0 s g^{-1}. Further increasing the amount of TPP added to 50 wt% does not obviously change the SET values, which is relevant to real TPP content, as observed during TGA results and XPS results. Considering a balance between fire retardancy and mechanical properties, we chose 25 wt% TPP in PI-TPP as our optimized CC substrate for subsequent demonstrations.

Second, we further studied the effect of composite CC thickness on flame retardancy. As shown in Fig. 3b, the value of SET substantially decreases when the thickness of PI-TPP-Cu increases from 5 μm to 9 μm. Even when the thickness is increased to 28 μm, the average specific mass of the PI-TPP-Cu CC is determined to be only ~3.39 mg cm^{-2} (Supplementary Fig. 10), which is still much lighter than the thinnest Cu CC (5.38 mg cm^{-2}, 6 μm thick) used in LIB. In this paper, a 9 μm thick PI-TPP-Cu CC was chosen for subsequent demonstrations. As shown in Fig. 3c and Supplementary Video 2, bare Cu/Gr electrode soaked with electrolyte is highly flammable and burns continuously until the electrolyte is fully exhausted. Moreover, the flame is bright and clear, demonstrating that the electrolyte is burning without any interference. For PI-Cu-based graphite electrodes (PI-Cu/Gr), the flame rapidly diminishes within 2 s and is completely extinguished in 3.5 s (Supplementary Video 3). The PI-TPP-Cu-based graphite electrode (PI-TPP-Cu/Gr) exhibits the best fire retardancy, whereby the flame is completely self-extinguished within 1.0 s. Moreover, the PI-TPP-Cu/Gr electrode appears to be burning weakly, because the flame is turbid and much shorter, as shown in Supplementary Video 4. As the temperature increases, TPP or TPP radicals can be released based on the follow mechanism: (1) The mismatched temperature coefficients of PI (~3–6 × 10^{-5} K^{-1}) and Cu (~16.6 × 10^{-6} K^{-1}) will result in breakage of the original planar structure and cause cracks during thermal runaway, which will release TPP or TPP radicals. (2) At temperatures above 244 °C (the boiling point of TPP), the flame retardant will be gasified and quickly released. (3) The TPP will decompose and generate phosphorus-containing free radicals such as $PO^{\bullet}$ and $PO_2^{\bullet}$, which then neutralize the highly active $H^{\bullet}$ and $HO^{\bullet}$ radicals released by the burning electrolyte or other flammable components[39].

Figure 3d shows the capacities of the half-cells with PI-TPP-Cu/Gr and Cu/Gr electrodes when paired with a lithium metal anode. The half-cells have similar initial capacities (based on Gr) of 412.7 and 416.2 mAh g^{-1}, respectively, and similar Coulombic efficiencies of 0.05 C in the first activated cycle. We note that many publications report specific capacity normalized only by the weight of the active materials, ignoring the heavy dead weight of inactive materials in the electrode[40]. Here, we compared the specific capacity of the Gr electrode based on the whole mass of the electrode, including the active materials, CC, conductive additive and binder. As shown in Fig. 3d, the discharge capacities of PI-TPP-Cu/Gr based on the whole electrode are much higher than those of Cu/Gr from 0.1 C to 1 C. At a rate of 0.5 C, the capacity of the PI-TPP-Cu/Gr electrode remains at 226.0 mAh g^{-1} and is much higher than that of the Cu/Gr electrode (146.8 mAh g^{-1}), representing a 54.0% improvement via our electrode design. Figure 3e,f shows the charge–discharge voltage profiles of the Cu/Gr and PI-TPP-Cu/Gr cells between 0.01 and 1.5 V. The voltage profiles of the PI-TPP-Cu/Gr electrodes exhibit typical electrochemical features of the Gr anode. Similar Coulombic efficiency and voltage curves demonstrate that the flame retardant in our CC design does not affect normal battery operation, as further indicated by linear sweep voltammetry plots (Supplementary Fig. 11) and the long cycle stability of the PI-TPP-Cu/Gr anode (Supplementary Fig. 12).

Welding behaviours and pouch cell performance

Since the deposited Cu layers on the PI-Cu and PI-TPP-Cu CCs are ultrathin, it is hard to directly weld them onto a commercial Ni tab. By bridging with a Cu foil, both the PI-Cu and PI-TPP-Cu CCs can be satisfactorily welded (Fig. 4a,b). Notably, the added TPP does not affect the welding performance of our CC design.

Traditional LIB are assembled with Cu foil and Al foil as anodic and cathodic CCs, respectively[41,42]. As a representative demonstration of the extension to commercial viability, we used the as-synthesized composite CCs to replace the traditional metal CCs for LIB. Cu and Al layers 500 nm thick are coated on a PI-based supporting film (PI or PI-TPP) as the anodic and cathodic CCs, respectively. The flame-retardant-embedded cathodic CC (PI-TPP-Al) contains the same flame retardant ratio (25 wt%) as the anodic PI-TPP-Cu CC, because they are made from the same PI-TPP supporting film (XRD characterization of PI-TPP-Al and the fire retardancy of PI-TPP-Al/lithium cobalt oxide (LCO) are provided in Supplementary Figs. 13 and 14). We then constructed lithium-ion full cells by coating the anode and cathode on the corresponding CC set, forming the following full cells: commercial Cu||Al CC, ultralight PI-Cu||PI-Al CC, and ultralight and fire-retarding PI-TPP-Cu||PI-TPP-Al CC.

To mimic practical LIB, we subsequently assembled pouch cells using the aforementioned welding method by using LCO and Gr as cathode and anode, respectively, as shown in Supplementary Fig. 15, and 2 cm^2 CC areas were reserved for electrode coating. The unused electrode area (the electrode connection part) was covered by tape to avoid unwanted lithium deposition (Fig. 4c,d). We then examined the electrochemical performance of the Gr-LCO full cells based on each set of CCs: Cu/Gr||LCO/Al, PI-Cu/Gr||LCO/PI-Al and PI-TPP-Cu/Gr||LCO/PI-TPP-Al (written in the form 'anodic CC/anode||cathode/cathodic CC').

Figure 4e compares the cycle performance of different LCO-Gr full cells at a rate of 0.5 C. The Cu/Gr||LCO/Al has an ~88.1% capacity retention with stable efficiency over 200 cycles. The discharge capacities (based on LCO) of PI-Cu/Gr||LCO/PI-Al and PI-TPP-Cu/Gr||LCO/PI-TPP-Al full cells are comparable to those of the Cu/Gr||LCO/Al cell. Even after 200 cycles, the capacity retentions of PI-Cu/Gr||LCO/PI-Al and PI-TPP-Cu/Gr||LCO/PI-TPP-Al full cells are still maintained at ~88.0% and ~87.2%, respectively. To objectively reflect the real specific energy of the batteries, we further calculated the specific energy of the full cells based on the same areal capacity. As can be seen from the right axis in Fig. 4e, the specific energy of a traditional Cu/Gr||LCO/Al full cell is ~256 Wh kg^{-1} at initial cycle and is maintained at ~226 Wh kg^{-1} after 200 cycles. Compared to a traditional Cu||Al CC, the use of our ultralight composite CC increases the specific energy of LCO-Gr LIB to ~296 Wh kg^{-1} at initial cycle and subsequently maintains it at ~261 Wh kg^{-1} after 200 cycles. These consistent cycles and high

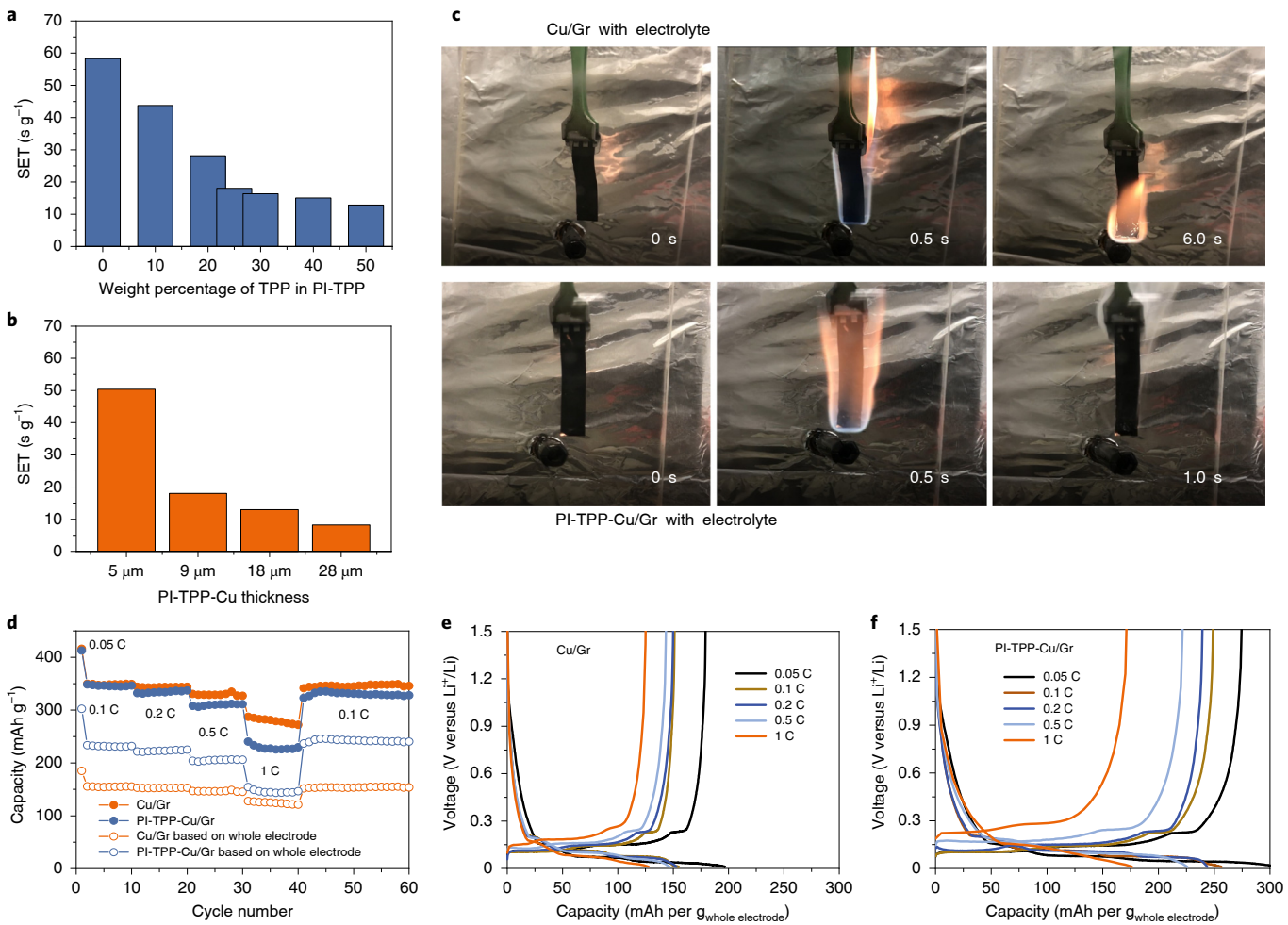

Fig. 3 | Fire retardancy behaviour and Gr anode performance based on different CCs. a,**b**, SET values of the PI-TPP-Cu/Gr electrode with electrolyte for different concentrations of TPP (actual amount added) in PI-TPP (**a**) and different thicknesses of PI-TPP-Cu CC (**b**). Each SET value is an average of three acquisitions. **c**, Photographs recording the burning test of the Cu/Gr (top row) and PI-TPP-Cu/Gr (bottom row) electrodes with electrolyte. The active material is Gr and the electrolyte is 1.0M $LiPF_6$ in EC/DEC (1:1, v/v). **d**–**f**, Rate performance (**d**) and corresponding galvanostatic charge–discharge voltage profiles (**e**,**f**) of the Cu/Gr and PI-TPP-Cu/Gr electrodes between 0.01 and 1.5 V, which show that the PI-TPP-Cu/Gr electrode has a higher discharge capacity based on the whole electrode than the Cu/Gr electrode from 0.1 C to 1 C.

Coulombic efficiencies (Supplementary Fig. 16) of PI-TPP-Cu/Gr||LCO/PI-TPP-Al full cells highlight that TPP is effectively sealed in the CC design and remains stable over prolonged cycling at room temperature.

To demonstrate the potential applicability in other LIB, we calculated the specific energy of LIB based on different types of cathode and anode. The whole cell mass (including cathode, anode, CC, conductive additive, binder, electrolyte and separator) was considered to evaluate the potential battery specific energy based on different CC pairs (Fig. 4f, detailed parameters and calculations are given in the Methods and Supplementary Tables 2–14).

We investigated the way in which battery specific energy is affected by CC thickness and electrode areal capacity. First, we compared the battery specific energy based on our composite CC and the thinnest Cu CC (6 μm) used so far under an areal capacity of 2 mAh cm^{-2}. Figure 4f shows the calculated specific energy of LIB based on LFP, LCO, NCM111, NCM532, NCM811 and NCA when paired with Gr and Si (specific abbreviations are listed below Supplementary Table 2). Replacing Cu||Al with PI-TPP-Cu||PI-TPP-Al CC leads to a notable increase in the specific energy of all battery systems of ~16–26%, which means that it is possible to achieve a specific energy higher than 400 Wh kg^{-1} based on conventional LIB. Second, we also compared the specific energy of LIB with different areal capacities from 2 mAh cm^{-2} to 4 mAh cm^{-2}. Even with a high areal capacity of 4 mAh cm^{-2} and the use of the thinnest CC (~6 μm), an improvement of specific energy from 8% to 13% can still be achieved. More importantly, LIB using our 9 μm thick composite CCs have a largely similar volumetric energy density, which is 99.1% of the volumetric energy density of the LIB fabricated using the commercial 6 μm thick Cu CC. Our design can also potentially be extended to decrease the PI-TPP-Cu thickness to 6 μm by further customizing the thickness of the embedded PI-TPP layer.

Full cell fire retardancy test

Fire exposure testing is one of the most extreme safety tests of LIB. To further investigate the battery safety performance of our PI-TPP-based CC, we carried out fire exposure testing of Cu/Gr||LCO/Al and PI-TPP-Cu/Gr||LCO/PI-TPP-Al full cells. Pouch cells with 120 mAh of LCO cathode were paired with Gr anodes and assembled as jelly rolls with commercial PP-PE-PP (25 μm) separators and 600 μl excess electrolyte (Fig. 5a). The cells were sealed in the glove box and subsequently left to rest for 24 h to ensure that the electrolyte had completely soaked the cells.

Upon exposure to an open flame, the Cu/Gr||LCO/Al pouch cell immediately ignites. The flame burns vigorously and spreads rapidly

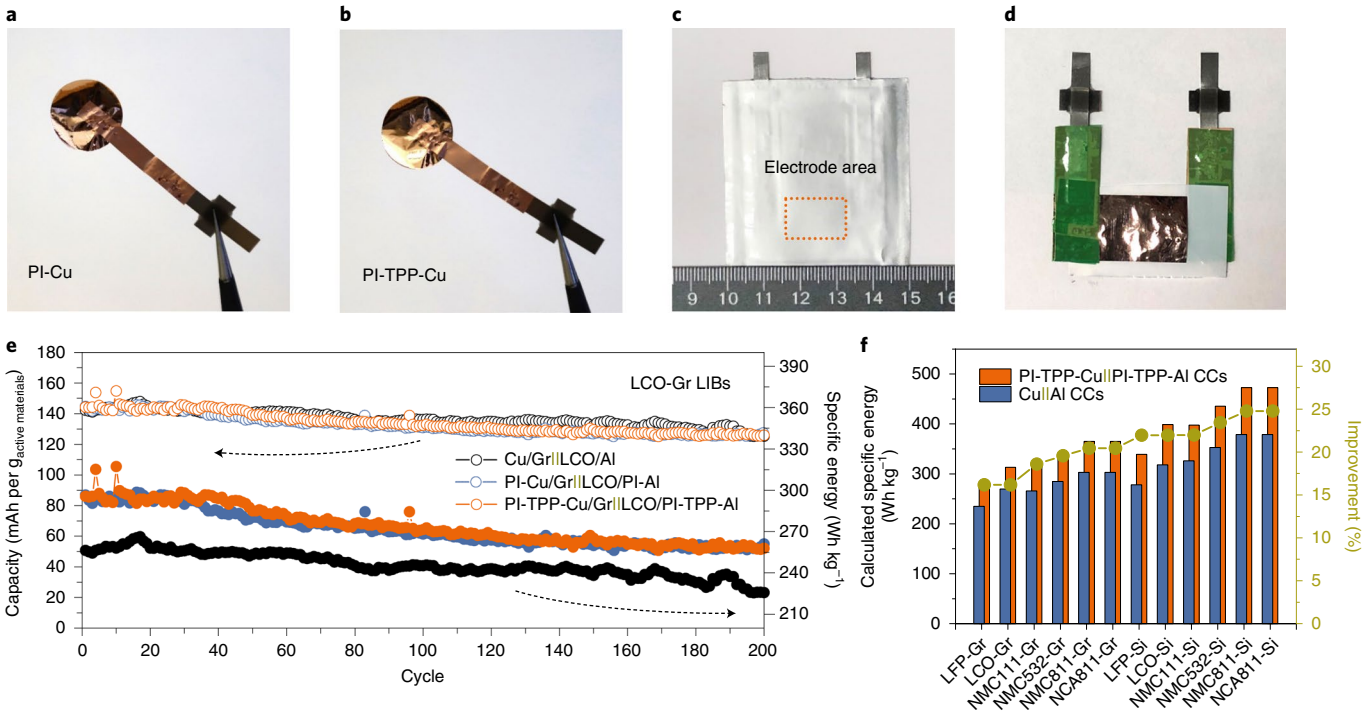

Fig. 4 | Electrochemical characterization of the full cells fabricated using conventional CCs and PI-based CCs. a,**b**, Digital camera photos showing the welding of PI-Cu (**a**) and PI-TPP-Cu (**b**) CCs onto copper foil. **c**,**d**, Digital camera photos showing the pouch cell assembled using a PI-based CC. The dotted rectangle in panel **c** is the electrode area. **e**, Galvanostatic cycling of Cu/Gr||LCO/Al (black), PI-Cu/Gr||LCO/PI-Al (blue) and PI-TPP-Cu/Gr||LCO/PI-TPP-Al (orange) full cells at 0.5 C. The top three curves are associated with the left *y* axis (indicated by the left-pointing dashed arrow) and the bottom three curves are associated with the right *y* axis (indicated by the right-pointing dashed arrow). The open circles represent the capacity calculated using the mass of the cathode active materials and the filled circles represent the capacity calculated using the whole battery mass (without packing). **f**, Specific energy of different LIB calculated based on commercial Cu||Al and PI-TPP-Cu|| PI-TPP-Al CCs. Blue and orange bars represent the specific energy ranges of batteries based on commercial Cu||Al CC pairs and PI-TPP-Cu||PI-TPP-Al CC pairs, respectively. The detailed cell parameters are in Supplementary Tables 2–14.

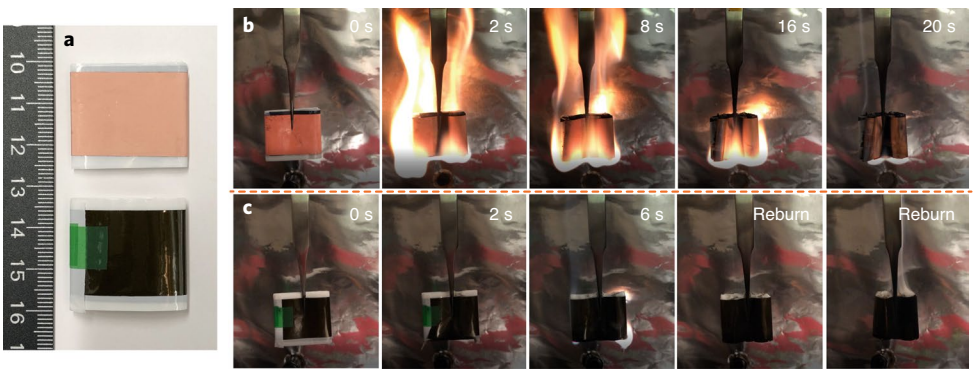

Fig. 5 | Fire retardancy test on full pouch cells assembled using Al/Cu CC and PI-TPP-Al/PI-TPP-Cu CC pairs. a, Photos of the assembled Cu/Gr||LCO/Al (top) and PI-TPP-Cu/Gr||LCO/PI-TPP-Al (bottom) pouch full cells. **b**,**c**, Flame retardancy test results for the Cu/Gr||LCO/Al (**b**) and PI-TPP-Cu/Gr||LCO/PI-TPP-Al (**c**) pouch full cells.

throughout the entire cell, as shown in Fig. 5b and Supplementary Video 5. The pouch cell based on traditional Al/Cu CC is completely burnt within 20 s. In contrast, the flame on the PI-TPP-Cu/Gr||LCO/PI-TPP-Al pouch cell burns weakly and rapidly self-extinguishes within about 6 s of ignition (Fig. 5c and Supplementary Video 6). More importantly, the flame appears much weaker than that of the control sample. Several subsequent reburnings of the pouch cells with our PI-TPP-based composite CC do not produce an obvious flame, and most of the pouch cell remains intact. The TPP in the pouch cell is important to impart flame-retardant properties by rapidly releasing phosphate-based free radicals to suppress the fire of a burning battery. However, based on the current results, we acknowledge that a comprehensive safety testing is needed in the future.

Conclusions

In summary, we successfully designed an ultralight and self-extinguishing current collector (CC) with improved specific energy and safer characteristics for LIB. This was achieved by replacing the traditional metal foil CC with a PI-TPP-Metal composite CC. The composite PI-TPP-Cu CC provides a fourfold decrease in density

while maintaining comparable mechanical properties to Cu foil. The specific energy of different LIB assembled using our CCs can generally be increased by ~16–26%, even compared to the specific energy obtained using the thinnest commercial Cu||Al CC. In contrast to previous implementations of in-cell flame retardants, our design whereby the flame retardant is encapsulated in the CC eliminates potential negative impacts on the electron/ion pathway and side reactions. Our strategy for the design of next-generation CCs holds enormous promise for practical battery applications by providing safer lithium batteries with even higher specific energies.

Methods

Synthesis of pure PI. In a typical synthesis, *N*,*N*-dimethylacetamide was used as solvent for the condensation polymerization of polyamic acid (PAA). 1,4-bis(4-amino-2-trifluoromethylphenoxy)benzene (6FAPB, 1.606 g, 3.75 mmol) and 4,4′-oxydianiline (4,4′-ODA, 0.751 g, 3.75 mmol) were added to dimethylacetamide (28 ml) in a 50 ml three-necked flask equipped with a mechanical stirrer, in which the molar ratio of 4,4-ODA to 6FAPB was 1:1. Because 4,4′-ODA is a suspected carcinogen, it needs special attention during synthesis. After being stirred for 0.5 h, pyromellitic dianhydride was added into the above solution under vigorous stirring. The molar ratio of diamines to dianhydride was 1:1.02. The reaction solution was gradually heated to 180 °C and maintained for 2 h to complete the polymerization. The honey-like, viscous PAA solution was then degassed for 5 min to remove the gas in the solution and subsequently coated on a clean glass substrate. Doctor blading was applied to coat the solution on the glass slides with various thicknesses. The coated films were dried overnight in the fume hood at room temperature and then removed from the glass substrate by cutting the four edges of the PAA films. As-obtained free-standing PAA films were finally imidized in a box furnace under air exposure to obtain PI films. The temperature ramping program was set as follows: (1) ramp up from 25 °C to 100 °C at 3 °C min^{-1}, (2) keep at 100 °C for 30 min, (3) ramp up to 200 °C at 3 °C min^{-1}, (4) keep at 200 °C for 30 min and (5) cool down to room temperature in the furnace.

Synthesis of PI-TPP. The synthesis process of PI-TPP was same as the PI synthesis process except that a fixed amount of TPP was added to the PAA solution. For 25% TPP in PI-TPP films, 0.45 g TPP was added.

Synthesis of PI-based current collectors. Before metal coating, the supporting film (either PI or PI-TPP) was treated with O_2 plasma for 5 min to graft hydrophilic functional groups onto the surface, which increases the interfacial adhesion[43,44]. Cu layers were deposited on treated PI or PI-TPP by pulsed DC magnetron sputtering using a Cu target under a protective argon atmosphere. The pressure of the sputter main chamber is less than 10^{-6} torr, and the target power was set to 200 W for Cu sputtering. To obtain a 500 nm thick Cu layer, a sputtering time of 1,800 s was applied. Similarly, Al layers were deposited on PI-TPP films by pulsed DC magnetron sputtering using an Al target under a protective argon atmosphere. The target power was also set to 200 W for Al sputtering. A series of composite anodic CCs (PI-Cu and PI-TPP-Cu) and composite cathodic CCs (PI-Al and PI-TPP-Al) were then achieved. Commercial Cu foil CCs and commercial Al foil CCs were used as control samples.

Electrode preparation and cell assembly. Gr was chosen as the anode material to estimate the performance of as-synthesized CCs. Standard slurry coating processes were applied to coat Gr onto the commercial Cu foil, PI-Cu and PI-TPP-Cu anodic CCs. Gr, Super P conductive carbon black and polyvinylidene fluoride were mixed in the weight ratio of 80:10:10 for slurry preparation, with *N*-methyl-2-pyrrolidone as solvent. The slurry was degassed and filtered by 200-mesh sieves before being coated on different CCs. A 2032 type coin cell was used, and 11 mm diameter electrodes were punched for the test for commercial Cu CCs. To fabricate Gr electrodes with PI-based CCs, 11 mm diameter supporting films (PI-Cu or PI-TPP-Cu) were punched and then Cu was sputtered on the surface. The electrode slurry was then coated onto the PI-based CCs. The electrolyte used was 1 M $LiPF_6$ in 50/50 (v/v) ethylene carbonate/diethyl carbonate (EC/DEC). Sandwiched polypropylene-polyethylene-polypropylene (Celgard 2325) was used as a separator. The counter electrode consisted of 750 µm thick lithium metal with 7/16 inch diameter. The cycling program was set as constant-current charging–discharging from 0.01 to 3.0 V (note that Fig. 3e,f only shows the charging–discharging curves between 0.01 and 1.5 V). LCO, Super P conductive carbon and polyvinylidene fluoride were mixed in an 80:10:10 mass ratio and dispersed in *N*-methyl-2-pyrrolidine, then coated onto commercial Al foil, PI-Al and PI-TPP-Al cathodic CCs. An initial cycle of 0.05 C was applied to optimally insert lithium ions into Gr and to form a stable solid electrolyte interphase layer on the Gr surface.

CC welding and LCO-Gr full cell assembly. In order to test the practical application of our composite CC, a ~2.0 cm^2 area of the CC was reserved for electrode coating. LCO and Gr were chosen as the cathodic and anodic active materials for demonstration, respectively. Before electrode coating, the four edges of the CC were covered by commercial PI films to form a controlled 2.0 cm^2 area for electrode coating. After the electrodes had completely dried, the edges of PI-Cu and PI-TPP-Cu CCs were welded with a Ni tab by bridging with a 12 µm thick Cu film, while the edges of PI-Al and PI-TPP-Al CCs were welded with an Al tab by bridging with a commercial Al film. For comparison, LCO and Gr were coated onto commercial Al and Cu foil, then directly welded onto Al and Ni tabs, respectively. Pouch cells were assembled based on each set of CCs: Al/LCO||Cu/Gr, PI-Al/LCO||PI-Cu/Gr, PI-TPP-Al/LCO||PI-TPP-Cu/Gr. The electrolyte used for pouch cell testing was 1 M $LiPF_6$ in 50/50 (v/v) EC/DEC. The average areal capacity of active materials in these pouch cells is 3.5 mAh cm^{-2}.The pouch cells were discharged and charged between 3.0 and 4.2 V at 0.5 C using an electrochemical station (LAND, Wuhan) to test their cycle lives. For all full cell testing, a five-cycle activation was applied before cycling to form a stable solid electrolyte interphase layer on the anodic surface.

Electrode and full cell flammability test. After the Gr electrodes were completely dried in a vacuum oven, we cut the electrodes into 1 cm × 5 cm strips. Vertical flame tests were performed on coated electrode materials on different CCs with a size of 1 cm × 5 cm. After 50 µl electrolyte was added, the electrode was sealed in a 20 ml vial to ensure the electrodes were completely wetted by the electrolyte. The fire from a gas burner was applied to the tested electrode. The SET values of relevant samples in consideration of the actual electrolyte mass remaining in the electrodes were calculated. For the LCO-Gr full cell flammability test, 120 mAh pouch cells were assembled based on each set of CCs: Al/LCO||Cu/Gr and PI-TPP-Al/LCO||PI-TPP-Cu/Gr. Celgard 2325 was used as a separator. After the pouch cells were assembled (2.5 cm × 2.0 cm, eight layers), 600 µl electrolyte was added and the cell was sealed to make sure the pouch cell was completely wetted by electrolyte. The mass loading of LCO and Gr in these pouch cells is ~20 mg cm^{-2} and ~12 mg cm^{-2}, respectively. In the flammability test, the pouch cell with electrolyte was exposed to a direct flame from a lighter. After the cells were ignited, the lighter was removed, and the time for the flame to self-extinguish was recorded.

Materials characterization. TGA was performed on a TA Instrument Q500 with a heating rate of 5 °C min^{-1} under simulated air atmosphere (20% oxygen + 80% argon). FTIR spectra were measured using an FTIR spectrometer (Model 6700, Thermo Scientific). SEM images were taken on a FEI XL30 Sirion scanning electron microscope. XPS experiments were performed on an SSI SProbe XPS spectrometer with an Al (Ka) source. The tensile stress and strain of different films were measured using a micro materials tester (Instron, USA). Each specimen was trimmed to a 10 mm width and a 50 mm length by laser cutting to form homogeneous edges and then tested at a rate of 50 mm min^{-1}.

Data availability

All relevant data are included in the paper and its Supplementary Information. Source data are provided with this paper.

Received: 3 March 2020; Accepted: 26 August 2020;
Published online: 15 October 2020

References

1. Chen, Y. et al. Reduced graphene oxide films with ultrahigh conductivity as Li-ion battery current collectors. *Nano Lett.* **16**, 3616–3623 (2016).
2. Zhang, H., Yu, X. & Braun, P. V. Three-dimensional bicontinuous ultrafast-charge and -discharge bulk battery electrodes. *Nat. Nanotechnol.* **6**, 277–281 (2011).
3. Li, Y. Q. et al. Lithium ion breathable electrodes with 3D hierarchical architecture for ultrastable and high-capacity lithium storage. *Adv. Funct. Mater.* **27**, 1700447 (2017).
4. Li, N., Chen, Z., Ren, W., Li, F. & Cheng, H.-M. Flexible graphene-based lithium ion batteries with ultrafast charge and discharge rates. *Proc. Natl Acad. Sci.* **109**, 17360–17365 (2012).
5. Sun, H. et al. Hierarchical 3D electrodes for electrochemical energy storage. *Nat. Rev. Mater.* **4**, 45–60 (2019).
6. Liu, B. et al. Hierarchical three-dimensional $ZnCo_2O_4$ nanowire arrays/carbon cloth anodes for a novel class of high-performance flexible lithium-ion batteries. *Nano Lett.* **12**, 3005–3011 (2012).
7. Yazici, M., Krassowski, D. & Prakash, J. Flexible graphite as battery anode and current collector. *J. Power Sources* **141**, 171–176 (2005).
8. Zhamu, A., Jang, B. Z. & Chen, G. Large-grain graphene thin film current collector and secondary batteries containing same. US patent 9,484,160 (2016).
9. Wang, S. et al. Aluminum chloride-graphite batteries with flexible current collectors prepared from earth-abundant elements. *Adv. Sci.* **5**, 1700712 (2018).
10. Liu, K., Liu, Y., Lin, D., Pei, A. & Cui, Y. Materials for lithium-ion battery safety. *Sci. Adv.* **4**, eaas9820 (2018).
11. Fan, X. et al. Non-flammable electrolyte enables Li-metal batteries with aggressive cathode chemistries. *Nat. Nanotechnol.* **13**, 715–722 (2018).
12. Wu, H., Zhuo, D., Kong, D. & Cui, Y. Improving battery safety by early detection of internal shorting with a bifunctional separator. *Nat. Commun.* **5**, 5193 (2014).

13. Liu, Y., Zhu, Y. & Cui, Y. Challenges and opportunities towards fast-charging battery materials. *Nat. Energy* **4**, 540–550 (2019).
14. Liu, K. et al. Extending the life of lithium-based rechargeable batteries by reaction of lithium dendrites with a novel silica nanoparticle sandwiched separator. *Adv. Mater.* **29**, 1603987 (2017).
15. Wang, Q. et al. Thermal runaway caused fire and explosion of lithium ion battery. *J. Power Sources* **208**, 210–224 (2012).
16. Ribière, P. et al. Investigation on the fire-induced hazards of Li-ion battery cells by fire calorimetry. *Energy Environ. Sci.* **5**, 5271–5280 (2012).
17. Yeon, D., Lee, Y., Ryou, M.-H. & Lee, Y. M. New flame-retardant composite separators based on metal hydroxides for lithium-ion batteries. *Electrochim. Acta* **157**, 282–289 (2015).
18. Yim, T. et al. Self-extinguishing lithium ion batteries based on internally embedded fire-extinguishing microcapsules with temperature-responsiveness. *Nano Lett.* **15**, 5059–5067 (2015).
19. Liu, K. et al. Electrospun core-shell microfiber separator with thermal-triggered flame-retardant properties for lithium-ion batteries. *Sci. Adv.* **3**, e1601978 (2017).
20. Yu, L., Miao, J., Jin, Y. & Lin, J. Y. A comparative study on polypropylene separators coated with different inorganic materials for lithium-ion batteries. *Front. Chem. Sci. Eng.* **11**, 346–352 (2017).
21. Baginska, M. et al. Autonomic shutdown of lithium-ion batteries using thermoresponsive microspheres. *Adv. Energy Mater.* **2**, 583–590 (2012).
22. Cui, Y. et al. A fireproof, lightweight, polymer–polymer solid-state electrolyte for safe lithium batteries. *Nano Lett.* **20**, 1686–1692 (2020).
23. Wang, J. et al. Fire-extinguishing organic electrolytes for safe batteries. *Nat. Energy* **3**, 22–29 (2018).
24. Nakagawa, H. et al. Application of nonflammable electrolyte with room temperature ionic liquids (RTILs) for lithium-ion cells. *J. Power Sources* **174**, 1021–1026 (2007).
25. Zeng, Z. et al. Non-flammable electrolytes with high salt-to-solvent ratios for Li-ion and Li-metal batteries. *Nat. Energy* **3**, 674 (2018).
26. Tsujikawa, T. et al. Characteristics of lithium-ion battery with non-flammable electrolyte. *J. Power Sources* **189**, 429–434 (2009).
27. Suo, L., Hu, Y.-S., Li, H., Armand, M. & Chen, L. A new class of solvent-in-salt electrolyte for high-energy rechargeable metallic lithium batteries. *Nat. Commun.* **4**, 1481 (2013).
28. Wang, J. et al. Superconcentrated electrolytes for a high-voltage lithium-ion battery. *Nat. Commun.* **7**, 12032 (2016).
29. Xia, L., Li, S.-L., Ai, X.-P., Yang, H.-X. & Cao, Y.-L. Temperature-sensitive cathode materials for safer lithium-ion batteries. *Energy Environ. Sci.* **4**, 2845–2848 (2011).
30. Balakrishnan, P., Ramesh, R. & Kumar, T. P. Safety mechanisms in lithium-ion batteries. *J. Power Sources* **155**, 401–414 (2006).
31. Chen, Z. et al. Fast and reversible thermoresponsive polymer switching materials for safer batteries. *Nat. Energy* **1**, 15009 (2016).
32. Wang, H., Wang, T., Yang, S. & Fan, L. Preparation of thermal stable porous polyimide membranes by phase inversion process for lithium-ion battery. *Polymer* **54**, 6339–6348 (2013).
33. Ma, P. et al. A review on high temperature resistant polyimide films: heterocyclic structures and nanocomposites. *Compos. Commun.* **16**, 84–93 (2019).
34. Li, J. et al. Synthesis and characterization of porous polyimide films containing benzimidazole moieties. *High. Perform. Polym.* **29**, 869–876 (2017).
35. Velencoso, M. M., Battig, A., Markwart, J. C., Schartel, B. & Wurm, F. R. Molecular firefighting—how modern phosphorus chemistry can help solve the challenge of flame retardancy. *Angew. Chem. Int. Ed.* **57**, 10450–10467 (2018).
36. Kränzlin, N., Ellenbroek, S., Durán-Martín, D. & Niederberger, M. Liquid-phase deposition of freestanding copper foils and supported copper thin films and their structuring into conducting line patterns. *Angew. Chem. Int. Ed.* **51**, 4743–4746 (2012).
37. Barnat, E., Nagakura, D., Wang, P.-I. & Lu, T.-M. Real time resistivity measurements during sputter deposition of ultrathin copper films. *J. Appl. Phys.* **91**, 1667–1672 (2002).
38. Xiao, J. et al. Fire retardant synergism between melamine and triphenyl phosphate in poly(butylene terephthalate). *Polym. Degrad. Stabil.* **91**, 2093–2100 (2006).
39. Granzow, A. Flame retardation by phosphorus compounds. *Acc. Chem. Res.* **11**, 177–183 (1978).
40. Liu, N. et al. A pomegranate-inspired nanoscale design for large-volume-change lithium battery anodes. *Nat. Nanotechnol.* **9**, 187–192 (2014).
41. Li, M., Lu, J., Chen, Z. & Amine, K. 30 years of lithium-ion batteries. *Adv. Mater.* **30**, 1800561 (2018).
42. Schmuch, R., Wagner, R., Hörpel, G., Placke, T. & Winter, M. Performance and cost of materials for lithium-based rechargeable automotive batteries. *Nat. Energy* **3**, 267–278 (2018).
43. Hong, J. H., Lee, Y., Han, S. & Kim, K.-J. Improvement of adhesion properties for Cu films on the polyimide by plasma source ion implantation. *Surf. Coat. Technol.* **201**, 197–202 (2006).
44. Kim, M.-H. & Lee, K.-W. The effects of ion beam treatment on the interfacial adhesion of Cu/polyimide system. *Met. Mater. Int.* **12**, 425–433 (2006).

Acknowledgements

This work was supported by the Assistant Secretary for Energy Efficiency and Renewable Energy, Office of Vehicle Technologies of the US Department of Energy under the eXtreme Fast Charge Cell Evaluation of Li-ion batteries (XCEL) program. We thank the Stanford Nano Shared Facilities (SNSF) and the Stanford Nanofabrication Facility (SNF) for SEM, FTIR, XPS, tensile strength characterizations and Lesker sputter fabrication.

Author contributions

Y. Ye and Y.C. conceived the concept. Y. Ye, Y.C. and Y.L. designed the experiments. Y. Ye and L.-Y.C. carried out the experimental works. Y. Ye and L.-Y.C. carried out the syntheses and performed material characterization, electrochemical measurements and flame retardancy tests. H.W., H.L., W.H., J.W. and K.L. assisted in the synthesis and characterization of materials. Y. Ye, Y.L., H.W., W.H., J.W., H.C., X.G. and S.C.K. helped with the data analysis. Y. Yang performed the SEM experiments. H.L. helped with the X-ray photoelectron spectroscopy measurement. A.Y. collected the FTIR spectra. X.X. helped with XRD experiments. Y. Ye and Y.C. wrote the paper. Y. Ye, W.H., G.Z, D.T.B. and W.Z. revised the paper. All authors contributed to the discussion of the manuscript.

Competing interests

The authors declare no competing interests.

Additional information

Supplementary information is available for this paper at https://doi.org/10.1038/s41560-020-00702-8.

Correspondence and requests for materials should be addressed to Y.C.

Reprints and permissions information is available at www.nature.com/reprints.

Publisher's note Springer Nature remains neutral with regard to jurisdictional claims in published maps and institutional affiliations.